



KOH-modified Ni/LaTiO₂N Schottky junction efficiently reducing CO₂ to CH₄ under visible light irradiation

Lei Lu^{a,1}, Zhenyu Xin^{a,1}, Xiaohui Wang^{a,1}, Shaomang Wang^a, Heng Zhu^a, Taozhu Li^a, Yaliu Gu^a, Shicheng Yan^{a,*}, Zhigang Zou^{a,b}

^a Jiangsu Key Laboratory of Artificial Functional Materials, Eco-materials and Renewable Energy Research Center (ERERC), National Laboratory of Solid State Microstructures, Collaborative Innovation Center of Advanced Microstructures, College of Engineering and Applied Sciences, Nanjing University, No. 22 Hankou Road, Nanjing, Jiangsu 210093, PR China

^b Jiangsu Province Key Laboratory for Nanotechnology, School of Physics, Nanjing University, No. 22 Hankou Road, Nanjing, Jiangsu 210093, PR China



ARTICLE INFO

Keywords:

Molecule activation
CO₂ reduction
Charge separation
Schottky junction

ABSTRACT

Efficiency of solar-driven CO₂ into fuels is largely limited by the sluggish reaction kinetics resulting from high activation barriers and poor electron-hole separation. Here, a synergistic strategy was proposed to overcome these obstacles. As a prototype, KOH-modified Ni/LaTiO₂N photocatalyst afforded a high performance in CO₂ reduction with a generation rate of 9.69 μmol g⁻¹ for CH₄ and 0.31 μmol g⁻¹ for CO, about 5 times higher than the catalytic activities of LaTiO₂N. The prominent enhancement results in the following effects: (1) Schottky barrier at Ni/LaTiO₂N interface boosts separation of electron-hole pairs. (2) The OH- of KOH as basic sites favors activation of CO₂ into CO₃²⁻ species, significantly improving the reaction kinetics of CO₂ reduction. (3) The OH- also functions as hole acceptor, boosting the proton release from H₂O oxidation.

1. Introduction

Converting CO₂ and H₂O into valuable fuels with solar energy has significant potential to address the worldwide energy and environmental issues [1–5]. However, the low energy efficiency limits the practical applications of this technique, as a result of sluggish kinetics in CO₂ activation and proton release from H₂O [6–8]. Meanwhile, the easy electron-hole recombination, in bulk as well as on surface of photocatalysts, limits the CO₂ conversion efficiency [9–11]. Therefore, to achieve efficient CO₂ reduction, decreasing activation barriers of the redox reactions and improving charge separation of the photocatalyst are urgently required.

It was well demonstrated that solid bases, such as MgO and NaOH, were able to activate CO₂ to carbonate species (CO₃²⁻) with lowered O–C–O bond angle and increase O–C bond length via chemisorption roles [12–14]. Very recently, spatially separated La₂O₃ solid base and oxygen vacancies could achieve simultaneous activation of CO₂ and H₂O into CO₃²⁻ and –OH species, respectively, leading to a two-fold enhancement in CH₄ yields over LaTiO₂N under visible light irradiation without any cocatalysts [15]. Notably, the separated active sites tended to induce the separation of the oxidation and reduction half reactions, thus helping to suppress reverse reaction and reduce recombination of

photogenerated charges. Nevertheless, built-in electric field is regarded as one of the most effective methods to separate charges, thus isolating the oxidation and reduction processes at two different sites [16–22]. For example, after modification of Bi particles, a surface band bending downward at junction region between n-type Ta₃N₅ and Bi particles was formed for reaching the thermodynamic equilibrium, owing to the lower work function of Bi (4.2 eV) than that of Ta₃N₅ (4.5 eV) [17]. Thereby, the photogenerated electrons would be quickly injected into Bi particles to take part the CO₂ reaction, while the holes would be confined on Ta₃N₅ surface to drive the H₂O oxidation, thus resulting in 5 times increase in CO₂ reduction efficiency. These evidences indicated that the activation of CO₂ and H₂O, together with efficient charge separation, are indeed important for efficient CO₂ conversion. However, there is a lack of methods to combine decreasing reaction barrier with improving charge separation.

Here, we developed a multifunctional KOH-modified Ni/LaTiO₂N photocatalyst to simultaneously activate CO₂ and H₂O by KOH and enhance charge separation by Schottky junction between Ni and LaTiO₂N. The relatively high work function of Ni (5.2 eV) could lead to a band bending upward at the interface junction region of Ni and LaTiO₂N. The resulting built-in electric field could boost the charge separation efficiency. The alkaline nature of KOH could improve the

* Corresponding author.

E-mail address: yscfei@nju.edu.cn (S. Yan).

¹ These authors contributed equally to this work.

CO_2 adsorption ability of the photocatalyst and easily form low-energy CO_3^{2-} species, and hence decreasing the reaction barrier. Moreover, the hydroxyl ion (OH^-) could also function as acceptor of holes, boosting the proton release from sluggish H_2O oxidation. As a result, the KOH-modified Ni/LaTiO₂N exhibited about 5-fold higher performance in CO_2 reduction than LaTiO₂N. The successful demonstration of synergistic effects of molecule activation and charge separation holds a potential application for efficient solar-to-hydrocarbon conversion.

2. Experimental section

2.1. Preparation of La₂Ti₂O₇ precursor

A molten-salt assisted method was used to synthesize the La₂Ti₂O₇ precursor. Typically, a stoichiometric mixture of La₂O₃ and TiO₂ was intensively mixed with a NaCl-KCl eutectic salt (mole ratio, NaCl: KCl = 1:1), according to the mole ratio 0.05:1 of La₂Ti₂O₇ to eutectic salt. Then, the resulting mixtures were heated to 1273 K at a rate of 100 K/h, and held at this temperature for 10 h. It was subsequently cooled down to 973 K at a rate of 50 K/h and then to room temperature naturally. The La₂Ti₂O₇ crystals were separated by deionized water washing and dried at 353 K overnight.

2.2. Preparation of Ni/LaTiO₂N photocatalyst

The LaTiO₂N was prepared by direct nitridation of La₂Ti₂O₇ under 500 mL/min flowing NH₃ at 1223 K for 12 h, followed by a natural cooling process to room temperature. To obtain the Ni/LaTiO₂N, the as-prepared LaTiO₂N was impregnated in Ni(NO₃)₂ solution and dried under vacuum. Then, the resulting mixture was held at 1023 K for 0.5 h under 500 mL/min flowing NH₃. The KOH (0.2% in mass) modified Ni/LaTiO₂N, denoted as Ni/LaTiO₂N-KOH, was prepared by a simple impregnation method, and followed by a vacuum drying process at 353 K overnight.

2.3. Materials characterization

The crystal phases were identified by X-ray diffraction (XRD, Rigaku Ultima III, Japan), and the X-ray diffractometer was operated at 20 kV and 40 mA with Cu-K α radiation. The particle morphology and size were examined by scanning electron microscopy (SEM, FEI Nova Nano SEM 230, USA). The crystallographic characteristics of the obtained crystals were analyzed by transmission electron microscopy (TEM, FEI Tecnai G2 F30 S-Twin, USA) operated at 200 kV. Diffused reflectance spectrum was scanned by a UV-vis spectrophotometer (UV-2500, Shimadzu Co., Japan) and transformed into absorption spectrum with Kubelka-Munk relationship. The specific surface area was measured from nitrogen (N₂) adsorption-desorption isotherm at 77 K by an automatic surface area analyzer (Micromeritics Tristar-3000, USA) after the samples had been dehydrated at 423 K for 2 h in the flowing N₂. The CO₂ adsorption was measured by the applied BET method at 273 K. The surface chemical species was investigated by X-ray photoelectron spectroscopy (XPS) on PHI5000 Versa Probe (ULVAC-PHI, Japan) with monochromatized Al K α X-ray radiation (1486.6 eV). The energy resolution of the electrons analyzed by the hemi-spherical mirror analyzer is about 0.2 eV. The C 1s core level at 284.6 eV was taken as an internal reference to correct the shift of the binding energies. The room temperature photoluminescence (PL) spectra were acquired using an objective-scanning confocal microscope system, in which the samples were excited through an oil-immersion objective lens (Olympus, SR-ASZ-0103, 150) using a 40 mW pulsed laser (488 nm).

2.4. Photocatalytic evaluation

The gas-phase CO₂ photoreduction was tested in a glass reactor with an area of 4.2 cm², and photocatalyst (40 mg) was uniformly dispersed.

The light source was a 300 W Xenon arc lamp fitted with a cutoff filter ($\lambda > 420$ nm). The volume of the reaction chamber was about 230 mL. Before irradiation, the reaction system was vacuumed several times, and then high-purity gas of compressed CO₂ (purity 99.999%) was introduced into the reaction chamber to achieve an ambient pressure. Subsequently, deionized water (0.4 mL) was injected into the chamber as reducing reactant. Prior to irradiation, the adsorption process was held for 2 h. During the reaction, 1 mL gas was extracted by a sampling needle from the chamber at given intervals for subsequent concentration analysis. The carbon-based products were quantified by a gas chromatography (GC-2014, Shimadzu Corp., Japan) with flame ionization detector (FID).

2.5. Computational calculations

The Cambridge sequential total energy package (CASTEP) code was used to perform the density functional theory (DFT) computations. The general gradient approximation (GGA) with PBE was used to describe the exchange-correlation effects for the calculations of work function and adsorption energy [17]. The attractive energy between nuclear and electrons was calculated by ultrasoft pseudo-potential. The convergence threshold of geometric optimization was set at 2.0×10^{-5} eV atom⁻¹ for total energy, 0.05 eV Å⁻¹ for maximum force, 0.1 GPa for stress and 0.002 Å for maximum displacement. For the calculations of work function, the structure of Ni (111) was built including 4 atoms of Ni, and lattice parameter was $a = b = 3.5$ Å, $c = 12.1$ Å and $\alpha = \beta = 90^\circ$, $\gamma = 120^\circ$. The structure of LaTiO₂N (002) contained 3 atoms of La, 3 atoms of Ti, 6 atoms of O, and 3 atoms of N, and lattice parameter was $a = 5.6$ Å, $b = 7.9$ Å, $c = 16.5$ Å, $\alpha = \beta = 90^\circ$, and $\gamma = 89.9^\circ$.

3. Results and discussions

3.1. Photocatalyst preparation and characterization

X-ray diffraction (XRD) analysis (Fig. S1a) indicated that the La₂Ti₂O₇ (JCPDS No. 70-1690) was completely converted into orthorhombic LaTiO₂N (JCPDS No. 48-1230) via the nitridation process. Scanning electron microscopy (SEM) observation (Fig. S1b) showed that the obtained LaTiO₂N was porous microplate (0.4–0.6 μm in thickness, 1.5–1.7 μm in width, and 3.5–4 μm in length). After heating mixture of LaTiO₂N and Ni(NO₃)₂ under NH₃, xNi/LaTiO₂N hybrids could be obtained, where the x represented the mole ratio between Ni and LaTiO₂N. As shown in Fig. 1a, when $x > 0.1$, XRD peaks of Ni crystals (JCPDS No. 04-0850) were well indexed, indicating a phase transformation from Ni(NO₃)₂ into Ni due to thermal reducibility of NH₃. Fig. 1b and c showed the SEM images of 0.1Ni/LaTiO₂N. Obviously, isolated particles randomly distributed on the plate-like LaTiO₂N surface, confirming the presence of Ni crystals. No visible changes in XRD patterns of LaTiO₂N were observed in Ni/LaTiO₂N (Fig. S1c).

Transmission electron microscopy (TEM) observations further confirmed the typical morphology of porous LaTiO₂N plates (Fig. 2a). The selected area electron diffraction (SAED) pattern with orderly diffraction spot showed that the LaTiO₂N was a single crystal (Fig. 2b). The measured lattice spacing of 0.39 nm in high-resolution TEM (HR-TEM) image was fixed for (002) plane of LaTiO₂N (Fig. 2c). Fig. 2d showed the representative TEM image of 0.2Ni/LaTiO₂N. As can be seen, the Ni nanoparticles closely contact with LaTiO₂N. This may give rise to form semiconductor-metal junction, thus promoting the electron transfer. As shown in SAED patterns of 0.2Ni/LaTiO₂N (Fig. 2e), well-aligned diffraction spot together with diffraction ring were observed, indicating that the Ni particles existed on the surface of LaTiO₂N. The Ni particles were also confirmed by the crystal lattice spacing of 0.21 nm for (111) facet of Ni, as illustrated in Fig. 2f. Fig. 2g showed the high-angle annular dark-field scanning transmission electron microscope (HAADF-STEM) image and corresponding elemental distribution of 0.2Ni/LaTiO₂N.

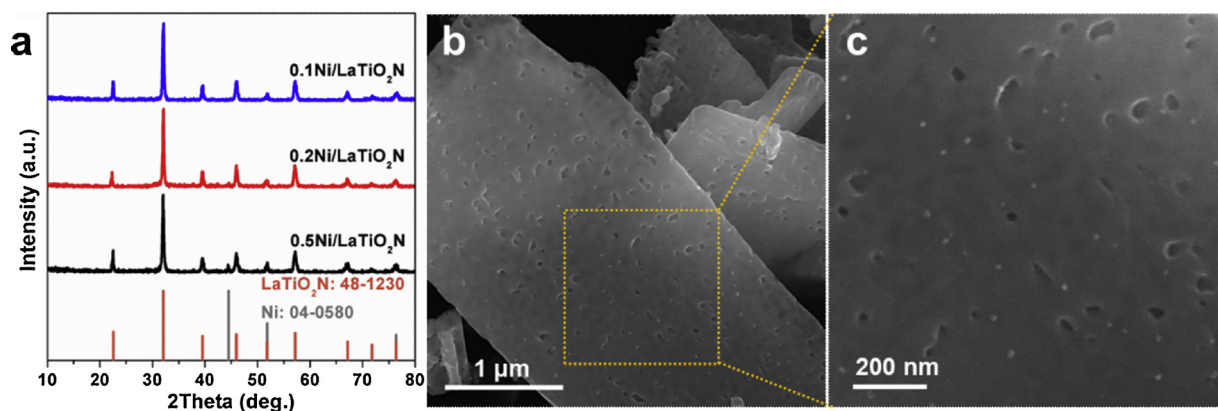


Fig. 1. (a) XRD patterns of $x\text{Ni/LaTiO}_2\text{N}$ samples ($x = 0.1, 0.2$, and 0.5). (b) SEM and (c) enlarged SEM images of $0.1\text{Ni/LaTiO}_2\text{N}$.

LaTiO₂N. It confirmed that nanoscale Ni particles randomly distributed on LaTiO₂N surface. Energy dispersive X-ray detector (EDX) analysis of 0.2Ni/LaTiO₂N showed that mole ratio of Ni to LaTiO₂N was 0.19:1 (Fig. S2), very closed to the nominal mole ratio.

The surface chemical states were analyzed by X-ray photoelectron spectroscopy (XPS). The binding energy at 66.4 eV for Ni 3p XPS spectrum of 0.2Ni/LaTiO₂N was assigned to Ni⁰ (Fig. 3a) [23,24], indicating that the Ni nanoparticles were in metallic state. The Ti 2p3/2

XPS spectrum of LaTiO₂N was deconvoluted into two peaks: 457.8 eV for Ti⁴⁺ and 456.7 eV for Ti³⁺ (Fig. 3b) [15,25]. The formation of Ti³⁺ defect was ineluctable during the nitridation process, resulting from partial reduction of Ti⁴⁺ at lattice of LaTiO₂N by NH₃ under high temperature. However, the content of Ti⁴⁺ slightly increased from 69.3% in LaTiO₂N to 70.3% in 0.2Ni/LaTiO₂N. The increased Ti⁴⁺ content indicated that the Ti³⁺ ions in LaTiO₂N tend to transfer electrons to Ni to form a Schottky junction, probably due to a compact

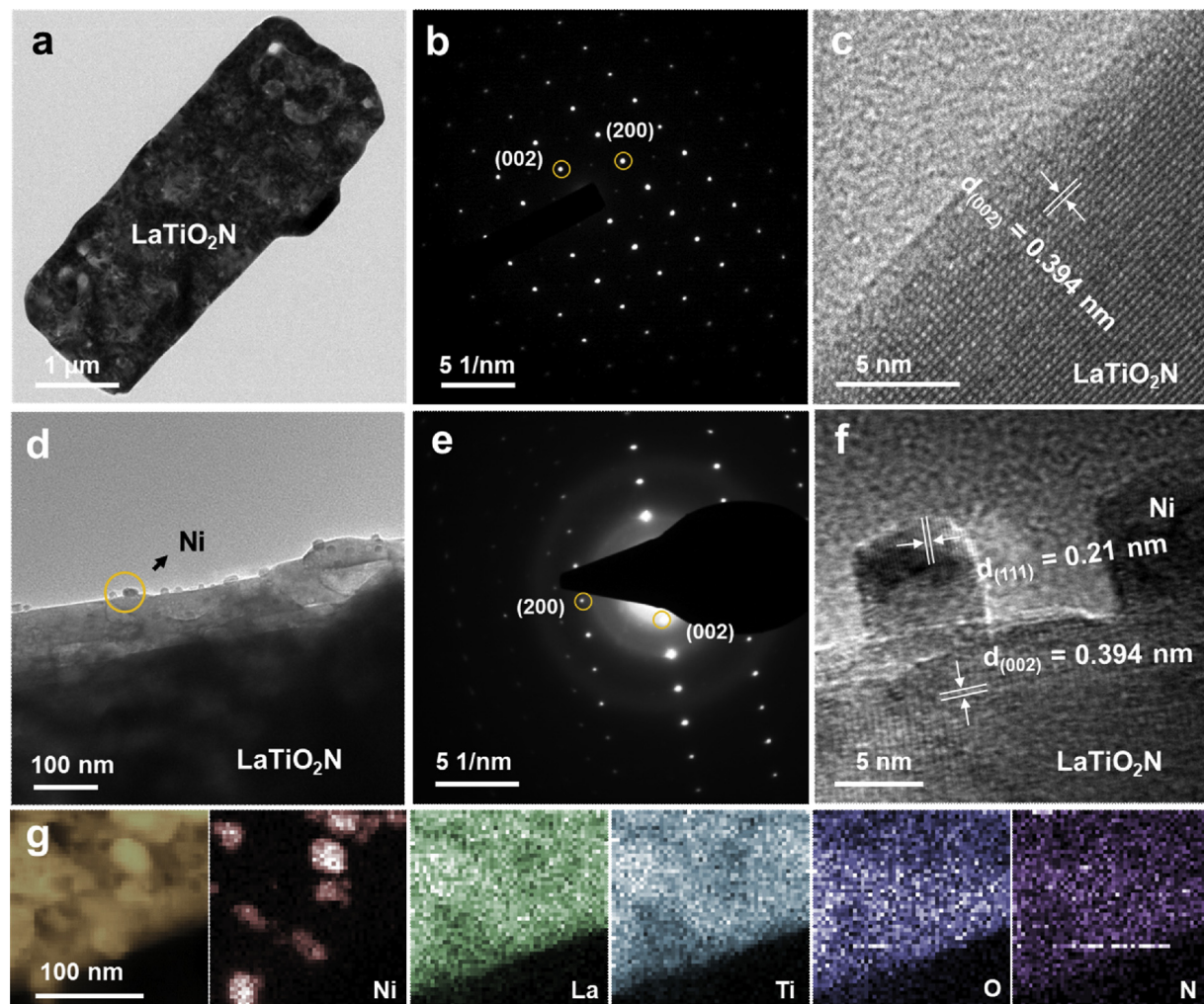


Fig. 2. (a) TEM, (b) SAED, and (c) HR-TEM images of LaTiO₂N. (d) TEM, (e) SAED, (f) HR-TEM, and (g) HAADF-STEM and corresponding elemental mapping images of 0.2Ni/LaTiO₂N.

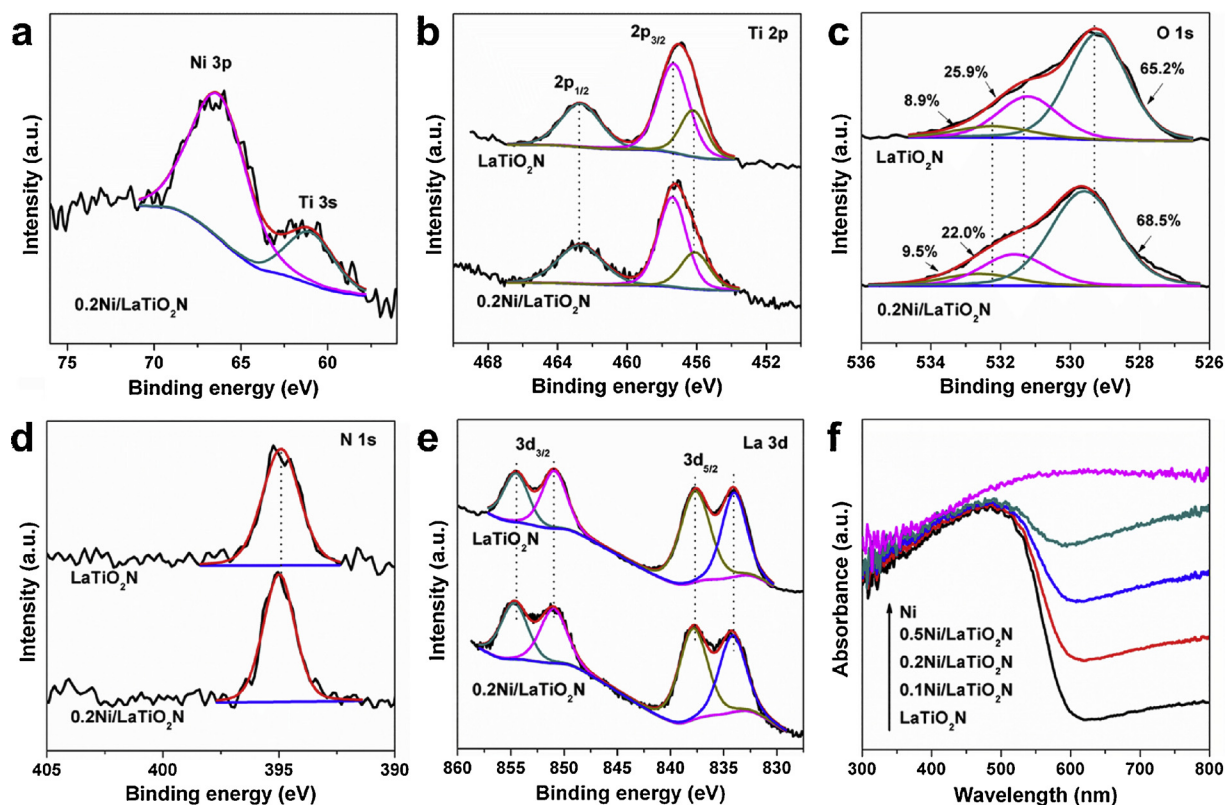


Fig. 3. (a) Ni 3p XPS spectra for 0.2Ni/LaTiO₂N, (b) Ti 2p, (c) O 1s, (d) N 1s, and (e) La 3d XPS spectra for LaTiO₂N and 0.2Ni/LaTiO₂N. (f) UV–vis absorption spectra for Ni, LaTiO₂N, and xNi/LaTiO₂N samples ($x = 0.1, 0.2$, and 0.5).

contact between Ni and LaTiO₂N. Indeed, a strong interface interaction could change surface chemical environment of the photocatalyst, thus affecting the photocatalytic performance possibly [25–28]. Such an effect was well demonstrated in the compact contact between LaTiO₂N and Ta₃N₅, causing the reduced Ti³⁺ defect in LaTiO₂N while increased Ta⁴⁺ defect in Ta₃N₅ [28].

Fig. 3c showed the O 1s XPS spectra of LaTiO₂N and 0.2Ni/LaTiO₂N. For LaTiO₂N, a peak at 531.2 eV was attributed to the lattice O atoms near O vacancies, resulting from charge balance when the Ti³⁺ occurred [29–31]. The peaks at 529.2 eV and 532.2 eV were respectively assigned to lattice O in LaTiO₂N and surface adsorbed O species [15,25]. Clearly, for 0.2Ni/LaTiO₂N, all three peaks in O 1s XPS were observed and exhibited about 0.4 eV chemical shift to higher binding energy. Moreover, about 3.9% decrease in concentration of O vacancies was observed in 0.2Ni/LaTiO₂N (22.0%) compared to LaTiO₂N (25.9%), confirming the decreased Ti³⁺ in LaTiO₂N after Ni modification. No obvious differences in N 1s XPS binding energy (Fig. 3d) were observed in LaTiO₂N (394.9 eV) and 0.2Ni/LaTiO₂N (395.0 eV) [17,25]. Hence, the obviously increased O lattice species confirmed the content decrease of Ti³⁺ and O vacancy defects in 0.2Ni/LaTiO₂N. For LaTiO₂N, in addition to the content decrease of Ti³⁺ and the binding energy increase of O, about 0.2 eV increase in binding energy of La 3d was found after the Ni modification (Fig. 3e) [35]. As is known, LaTiO₂N is an n-type semiconductor, and its Fermi level located near the conduction band minimum (CBM), and hence the work function is estimated to be about 4.7 eV [25,32]. The relatively larger work function of bulk Ni (5.2 eV) would induce a charge carrier diffusion from LaTiO₂N to Ni to reach the thermodynamic equilibrium [33,34]. Indeed, compared with Ni metal particles (67.2 eV) by direct Ni(NO₃)₂ reduction under NH₃ (Fig. S3), about 0.8 eV chemical shift to lower binding energy was observed for Ni 3p in Ni/LaTiO₂N (66.4 eV). These chemical shifts in Ni 3p, O 1s, Ti 3d, and La 3d would confirm the charge transfer between Ni and LaTiO₂N.

To further check the effects of Ni modification, the UV–vis absorption spectra were measured. As shown in Fig. 3f, the LaTiO₂N showed a main absorption edge up to 600 nm. A trail absorption after 600 nm was originated from the defect absorption, such as reduced Ti species and O vacancies [15,29,31]. Apparently, after Ni modification, the trail absorption intensity of Ni/LaTiO₂N increased with increasing the Ni mole ratio. The XPS results have shown that after Ni modification the Ti³⁺ and O vacancies defects in LaTiO₂N decreased significantly. Therefore, the increased trail absorption in Ni/LaTiO₂N cannot be attributed to the increased defect absorption. Usually, the metal nanoparticles show strong light absorption due to their plasma resonance effect. Indeed, the Ni nanoparticles from direct reduction of Ni(NO₃)₂ under NH₃ showed a remarkable light absorption in the wavelength range of 300–800 nm. This was due to its wide-spectrum range of localized surface plasmonic resonance (LSPR), thus enhancing the absorption ability and broadening the light response range for Ni/LaTiO₂N hybrids [36–38].

3.2. Photocatalyst CO₂ reduction test

The photoinduced CO₂ reduction was tested over the as-prepared LaTiO₂N and xNi/LaTiO₂N using H₂O as reagent under visible light ($\lambda \geq 420$ nm) irradiation by a 300 W Xe lamp. Before irradiation, adsorption equilibrium of CO₂ and H₂O molecules was carried out for 2 h, and no any products could be detected under dark condition. During irradiation, only CH₄ and CO could be detected. Fig. 4a and b respectively showed the typical CH₄ and CO yields of the time courses during the CO₂ reduction reaction. It can be seen that their yields were both increased with prolonging the irradiation time, thus convincing that the CO₂ reduction was driven by the photocatalysis in the presence of LaTiO₂N. After visible light irradiation for 6 h, the LaTiO₂N showed yield rate of 1.77 $\mu\text{mol g}_{\text{cat}}^{-1}$ for CH₄ and 0.51 $\mu\text{mol g}_{\text{cat}}^{-1}$ for CO. Compared to LaTiO₂N, the 0.2Ni/LaTiO₂N exhibited about 4 times increase in CH₄ generation (7.38 $\mu\text{mol g}_{\text{cat}}^{-1}$) and about 3 times decrease in CO

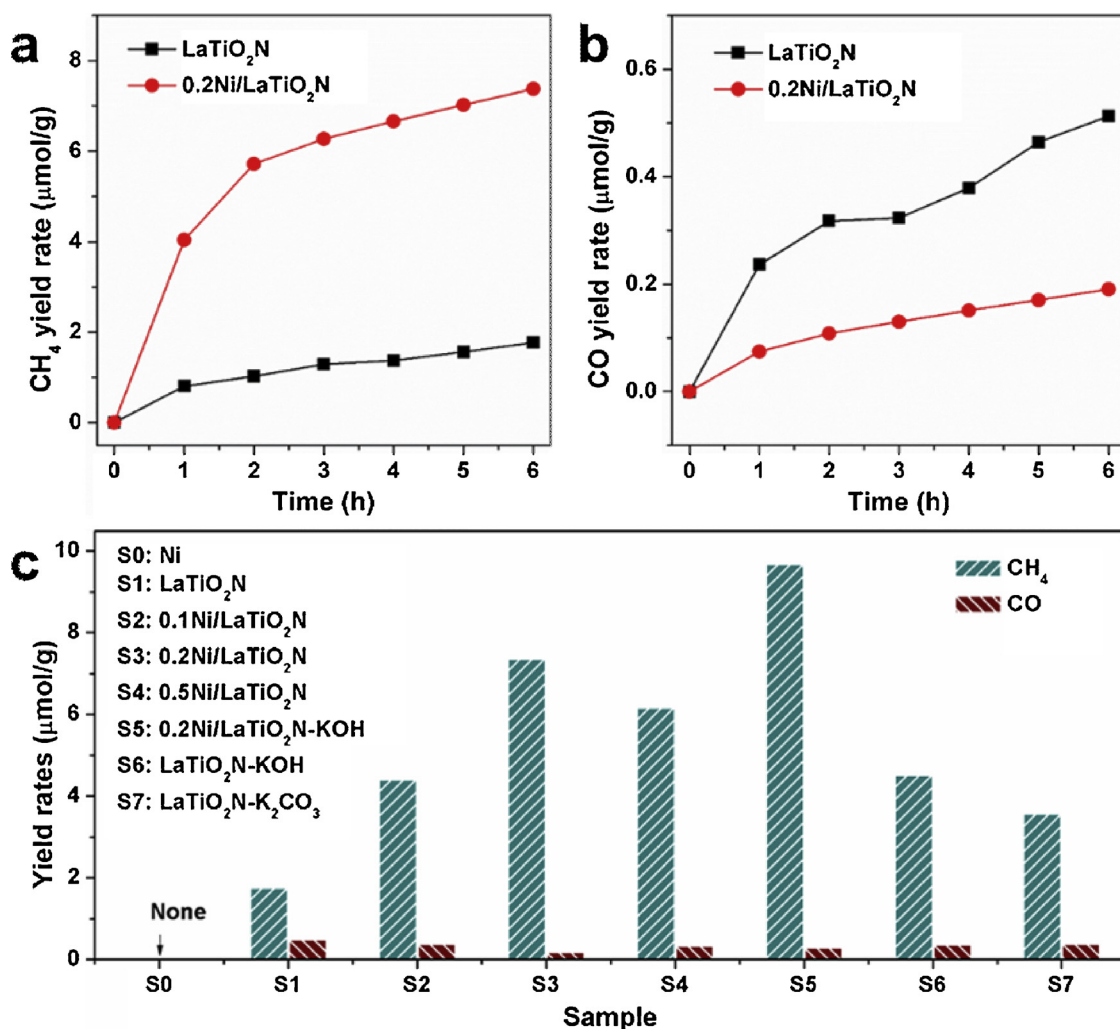


Fig. 4. (a) CH₄ and (b) CO generation for LaTiO₂N and 0.2Ni/LaTiO₂N. (c) Product generation for Ni, LaTiO₂N, xNi/LaTiO₂N ($x = 0.1, 0.2$, and 0.5), 0.2Ni/LaTiO₂N-KOH, LaTiO₂N-KOH, and LaTiO₂N-K₂CO₃.

product ($0.19 \mu\text{mol g}_{\text{cat}}^{-1}$), respectively. As is well known, eight electrons are required for CH₄ formation, while the CO generation is a two-electron process [17]. Therefore, despite of the decreased CO yield, the greatly increased CH₄ product for 0.2Ni/LaTiO₂N indicated that more photogenerated electrons could take part into the CO₂ reduction when the Ni particles were modified on the surface of LaTiO₂N. Notably, no CH₄ or CO generated on Ni particles alone (Fig. 4c), validating that Ni modification was exactly beneficial for promoting the photocatalytic CO₂ reduction efficiency of LaTiO₂N. As can be seen, Ni 3p XPS analysis showed a little differences before and after the CO₂ reaction (Fig. S3c), therefore, the relatively slow reaction rate after 1 h irradiation was possible due to the adsorption of intermediates formed on photocatalyst surface during the reaction process, thus making the reaction sites less active [15].

Modification of metal on photocatalyst surface commonly has positive impacts on charge separation or transfer process, thus improving the photocatalytic CO₂ reduction capacity [5,17]. In our case, the compact contact between Ni and LaTiO₂N, as observed by TEM, favors for formation of semiconductor-metal junction. The theoretical calculations were performed to understand the charge separation at the interface between Ni and LaTiO₂N. Surface slab model of highly exposed LaTiO₂N (002) and Ni (111) facets were built based on TEM observations (Fig. 5). Surface potential analysis demonstrated that the work function of Ni (111) was approximately 4.4 eV, evidently higher than 3.6 eV of LaTiO₂N (002). From the view of thermodynamics, charge

carrier could diffuse from LaTiO₂N to Ni due to the large work function of Ni. This would induce a surface band bending upward at the interface between LaTiO₂N and Ni, thus forming a space charge region that serves as a Schottky-type barrier for photogenerated electrons [33,39].

To experimentally estimate the charge separation, measurement of PL spectra was then conducted. An emission peak at 670 nm was observed in LaTiO₂N (Fig. 6a). Clearly, the 0.2Ni/LaTiO₂N hybrids showed a much lower PL emission peak intensity, denoting that the recombination of electrons and holes was decreased [17,25]. As a result, more electrons and holes were effective and capable to take part into the CO₂ reduction reaction and H₂O oxidation, respectively. Excellent charge separation could also be evaluated by photoelectrochemical methods. Fig. 6b showed the current-potential curves. As can be seen, the LaTiO₂N photoanode, assembled by LaTiO₂N particles through electrophoretic deposition on a fluorine-doped tin oxide (FTO) substrate (denoted as FTO|LaTiO₂N), exhibited a photocurrent density of about 1.1 mA cm^{-2} at $1.6 \text{ V}_{\text{RHE}}$. Obviously, the subsequent Ni modification by electrodeposition (10 mC cm^{-2} , denoted as FTO|LaTiO₂N|Ni) twofold increased the photocurrent (about 2.2 mA cm^{-2} at $1.6 \text{ V}_{\text{RHE}}$). SEM and TEM observations (Fig. S4) showed that the as-prepared Ni particles by electrodeposition are spheroidal particles with exposure of the (111) facets, and were randomly distributed on LaTiO₂N surface, similar to the Ni/LaTiO₂N powders. Therefore, we believe that the improvement in photocatalytic activity of FTO|LaTiO₂N|Ni and Ni/LaTiO₂N photocatalyst follows the same mechanism.

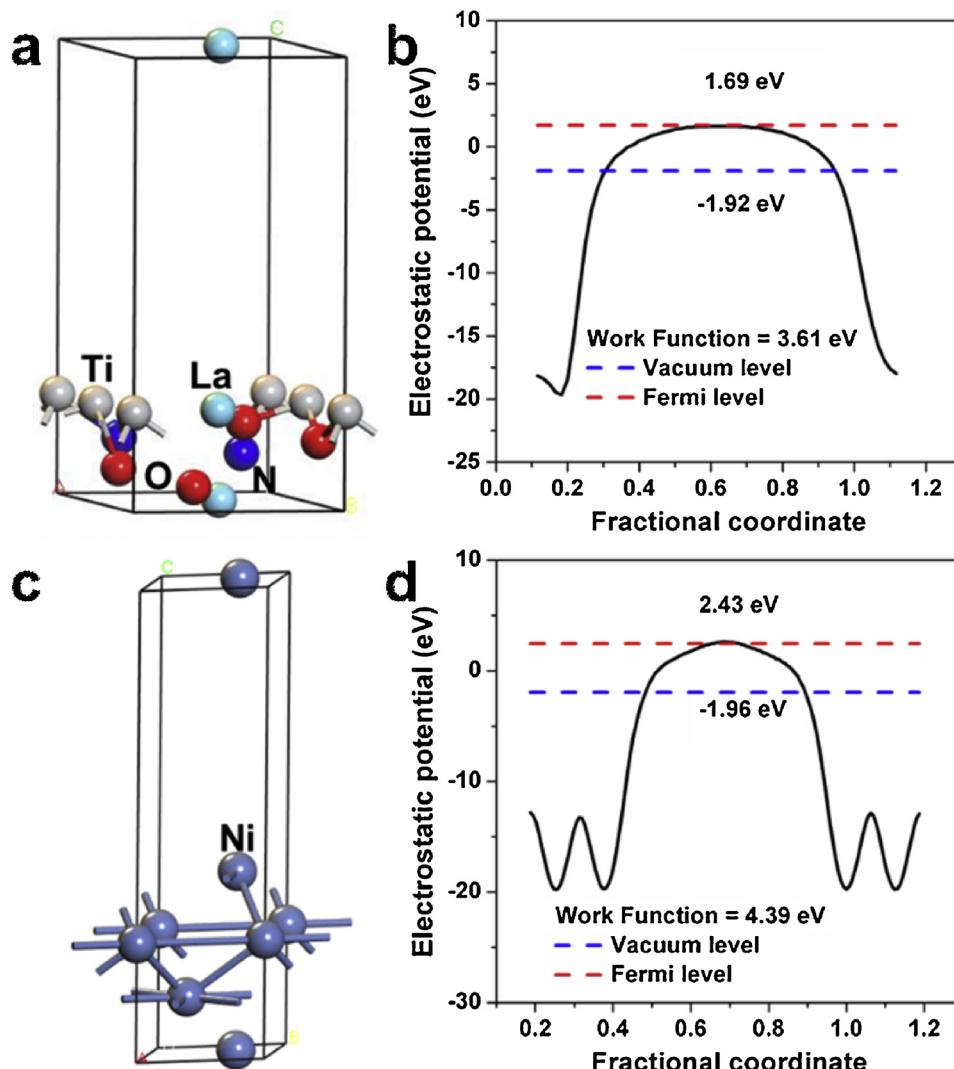


Fig. 5. (a) Surface slab models and (b) the calculated work function of LaTiO₂N (002) facet. (c) Surface slab models and (d) the calculated work function of Ni (111) facet.

Loading Ni on surface of LaTiO₂N could motivate more electrons transferring to the FTO conductive substrate, originating from the enhanced band bending upward after Ni modification and hence more holes and electrons could be separated (Fig. 6c). Therefore, an efficient charge separation resulting from Ni/LaTiO₂N junction was responsible for the enhanced CO₂ reduction.

To further check the junction effects, the FTO|Ni|LaTiO₂N electrode was prepared by electrodepositing Ni (10 mC cm⁻²) and LaTiO₂N on FTO in turn. The result showed that photocurrent of FTO|Ni|LaTiO₂N electrode was only 0.6 mA cm⁻² at 1.6 V_{RHE}. Especially, the photocurrent at before 0.6 V_{RHE} was negligible. This indicated that the charge separation at interface of LaTiO₂N-electrolyte junction is not as effective as at interface of LaTiO₂N-Ni junction. Such a similar result was obtained by assembling the LaTiO₂N particles on the Au back-electrode with high work function (5.1 eV) [33]. This confirmed that the surface band bending upward at the LaTiO₂N-Ni interface would restrict the photogenerated electrons to move from LaTiO₂N to Ni and be responsible for the accelerative hole transfer to Ni particles. It should be noted that, during the measurement of photocurrent, surface Ni layer (less than 4 nm in depth) was inevitably oxidized into NiOOH [40]. However, the high work function of NiOOH (5.9 eV) did not change the band bending upward in nature [41]. Therefore, the photoelectrochemical results provided valuable guidance for understanding the

charge separation underneath the Schottky junction. As a result, the spatially separated electrons and holes would induce the separation of CO₂ reduction and H₂O oxidation reaction on LaTiO₂N and Ni surface, respectively, thus inducing the enhanced CO₂ reduction efficiency.

With increasing the Ni amount, the CH₄ yields increased first and then decreased, resulting in a typical volcano-type distributions for CH₄ generation (Fig. 4c). In the xNi/LaTiO₂N samples, when $x \leq 0.2$, the gradually increased CO₂ reduction efficiency could be attributed to the increase in space charge region with increase of Ni amount, improving charge separation and thereby enhancing the CO₂ reduction efficiency. When $x > 0.2$, significantly decreased electron-hole recombination was attributed to the further increased space charge region, as demonstrated by PL spectra for 0.5Ni/LaTiO₂N (Fig. 6a). However, the highly loading amount of Ni on surface of LaTiO₂N would restrain the light absorption of LaTiO₂N because the preferential light absorption by Ni in the 300–800 nm region, as observed by UV-vis absorption spectra (Fig. 3f). This would decrease the generation of excited electrons and holes from LaTiO₂N, thus decreasing CO₂ conversion rate. Under visible light irradiation, all the Ni/LaTiO₂N hybrids showed evidently higher CO₂ reduction efficiency than LaTiO₂N, and the 0.2Ni/LaTiO₂N exhibited almost 4-fold higher CH₄ evolution than LaTiO₂N, giving solid evidence to support the benefits of Ni modification.

To further improve the CO₂ reduction efficiency, KOH modification

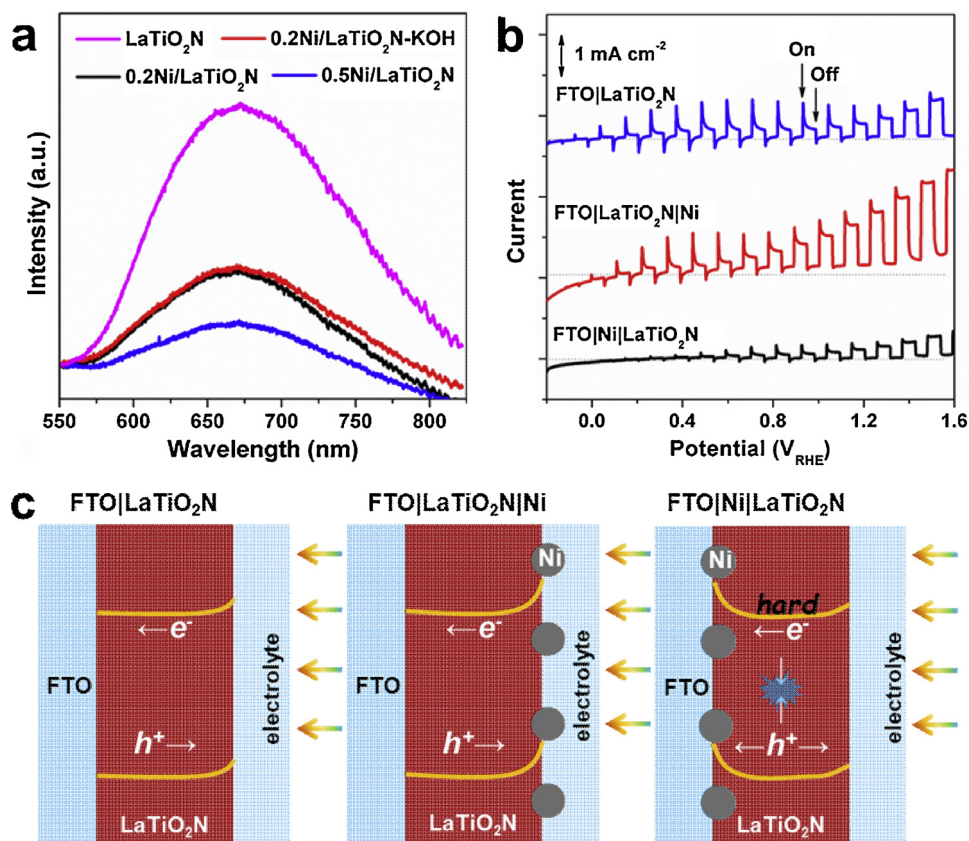


Fig. 6. (a) PL spectra for LaTiO₂N, 0.2Ni/LaTiO₂N, LaTiO₂N-KOH, and 0.2Ni/LaTiO₂N-KOH. (b) Current-potential curves and (c) illustrations of charge transfer for different LaTiO₂N photoanodes.

was loaded on 0.2Ni/LaTiO₂N by an immersion method. After 6 h irradiation, the CH₄ (9.69 μmol g_{cat.}⁻¹) and CO (0.31 μmol g_{cat.}⁻¹) yields on 0.2Ni/LaTiO₂N-KOH were 1.31 and 1.63 times higher than those (CH₄: 7.38 μmol g_{cat.}⁻¹, CO: 0.19 μmol g_{cat.}⁻¹) on the 0.2Ni/LaTiO₂N, respectively (Fig. 4c). XRD analysis, UV-vis absorption spectra, and Bruner-Emmet-Teller (BET) tests revealed almost no differences (Fig. S5) in crystal phase, light absorption, and specific surface areas for 0.2Ni/LaTiO₂N (23.21 m² g⁻¹) and 0.2Ni/LaTiO₂N-KOH (23.03 m² g⁻¹). The CO₂ adsorption tests by BET method at 273 K (Fig. 7a) indicated that CO₂ adsorbed on surface of 0.2Ni/LaTiO₂N-KOH (15.87 mg g⁻¹) was almost two times higher than that on the 0.2Ni/LaTiO₂N (7.89 mg g⁻¹) due to the strong alkaline nature of KOH. The similar PL spectra for 0.2Ni/LaTiO₂N and 0.2Ni/LaTiO₂N-KOH showed that the KOH modification does not change the recombination rate of photogenerated charges (Fig. 6a). The further enhanced CO₂ reduction efficiency would be attributed to the enhanced CO₂ adsorption on 0.2Ni/LaTiO₂N sample with the modification of KOH.

As demonstrated in the previous reports, the solid base could chemically adsorb and activate the CO₂ molecule into CO₃²⁻ species, thus decreasing the reaction barrier and promoting the CO₂ reduction [12–15]. To check the CO₂ chemisorption role of KOH, quantitative Fourier transform infrared (FT-IR) spectroscopy analysis was performed on 0.2Ni/LaTiO₂N and 0.2Ni/LaTiO₂N-KOH after the CO₂ adsorption-desorption equilibrium for 2 h under dark condition. For 0.2Ni/LaTiO₂N, two bands at 1658 and 1627 cm⁻¹ were assigned to the symmetric vibration of HCO₃⁻ species, while the bands at 1556, 1498, 1486, 1391, and 1371 cm⁻¹ were ascribed to CO₃²⁻ species (Fig. 7b) [42–44]. Clearly, the CO₃²⁻ species on 0.2Ni/LaTiO₂N-KOH obviously increased, confirming that the KOH modification could promote the CO₂ activation. During the light-driven CO₂ reduction, the abundant CO₃²⁻ species was generated on 0.2Ni/LaTiO₂N-KOH, suggesting a sustainable CO₂ activation by KOH. Notably, the amount of CO₃²⁻ species was

much higher than that of the HCO₃⁻ species during dark CO₂ adsorption or light reaction, demonstrating that the CO₃²⁻ species was the main active species for CO₂ reduction. An additional experiment, loading K₂CO₃ on LaTiO₂N (denoted as LaTiO₂N-K₂CO₃), was performed to confirm the effects of KOH. After 6 h irradiation, the CH₄ yield on LaTiO₂N-K₂CO₃ is 3.58 μmol g_{cat.}⁻¹ (Fig. 4c), which is much higher but slightly lower than CH₄ yields on LaTiO₂N (1.77 μmol g_{cat.}⁻¹) and LaTiO₂N-KOH (4.53 μmol g_{cat.}⁻¹), respectively. This evidence means that the CO₃²⁻ is able to accelerate the reaction kinetics.

In addition to the activation effect of KOH on CO₂, the OH⁻ ions in KOH may help the H₂O oxidation for providing protons and thus the CO₂ reduction efficiency [12,45]. To verify this fact, photocurrents of FTO|LaTiO₂N|Ni photoanodes using NaOH electrolyte with different pH values were obtained. As presented in Fig. 7c, the photocurrent at 1.0 V_{RHE} increased significantly as the pH value rises from 8.5 to 13.6, suggesting that high-concentration OH⁻ can accept the photogenerated holes to release protons more easily in kinetics. It was well known that the reduction of CO to CH₄ was achieved via a continuous methylation of CO by protons [25]. Therefore, we performed a photocatalytic reaction of CO and H₂O to CH₄ on LaTiO₂N-KOH to further check the positive role of KOH in proton supply from H₂O oxidation. Obviously, LaTiO₂N-KOH showed a CH₄ generation rate of 1.94 μmol g⁻¹ h⁻¹ (Fig. 7d), much higher than that over LaTiO₂N (0.58 μmol g⁻¹ h⁻¹), confirming the effect of OH⁻ on boosting proton release from H₂O oxidation.

On basis of the mentioned-above results, the probable CO₂ reaction process was as follows: Ni particles on LaTiO₂N surface induced a Schottky barrier. Under irradiation, the photogenerated electrons and holes of LaTiO₂N would be separated efficiently due to the resulting built-in electric field. Thus, the H₂O oxidation and CO₂ reduction were spatially isolated, helping to inhibit reverse reaction. The OH⁻ in KOH as basic sites favored CO₂ chemisorption into CO₃²⁻ species,

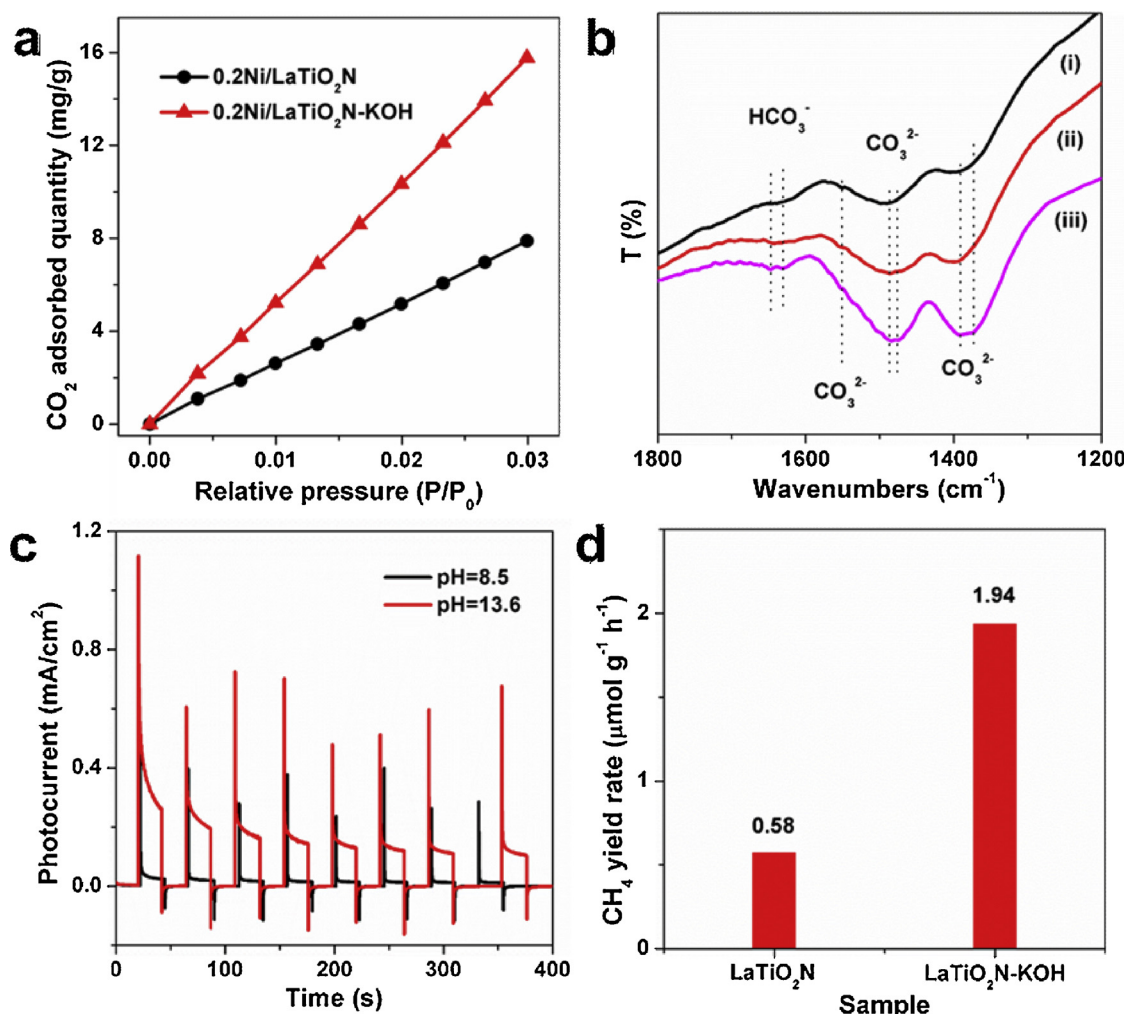


Fig. 7. (a) CO₂ adsorption isotherms for LaTiO₂N, 0.2Ni/LaTiO₂N, 0.2Ni/LaTiO₂N-KOH, and Ni. (b) FT-IR spectra for 0.2Ni/LaTiO₂N after CO₂ adsorption for 2 h (i spectrum), and 0.2Ni/LaTiO₂N-KOH after CO₂ adsorption for 2 h (ii spectrum) and reduction for 6 h (iii spectrum). (c) Photocurrents of LaTiO₂N photoanode in NaOH electrolyte at a bias of 1.0 V vs RHE. (d) CH₄ yield over LaTiO₂N with CO as the carbon source under visible light.

significantly contributed to both the bending of O—C—O bond and the decrease of the lowest unoccupied molecule orbit energy of CO₂. And, the OH[−] also could function as acceptor of holes, boosting the proton release from sluggish H₂O oxidation to accelerate CO₂ reduction.

4. Conclusions

In summary, a remarkably improved CO₂ photoreduction was demonstrated over KOH modified Ni/LaTiO₂N junction. The resulting built-in electric field at interface between Ni and LaTiO₂N boosted separation of electron-hole pairs. The OH[−] in KOH as basic sites favors CO₂ chemisorption into CO₃²⁻ species, significantly contributed to both the bending of O—C—O bond and the decrease of the lowest unoccupied molecule orbit energy of CO₂. And, the OH[−] also functions as acceptor of holes, boosting the proton release from sluggish H₂O oxidation. The successful demonstration of synergistic effects of CO₂ activation and charge separation provides a potential application for efficient solar-to-hydrocarbon conversion.

Acknowledgement

This work was supported primarily by the National Natural Science Foundation of China (51872135, 51572121, 21603098, and 21633004), the Natural Science Foundation of Jiangsu Province (BK20151265, BK20151383, and BK20150580), the Postdoctoral

Science Foundation of China (2017M611784) and the Fundamental Research Funds for the Central Universities (021314380133 and 021314380084).

Appendix A. Supplementary data

Supplementary material related to this article can be found, in the online version, at doi:<https://doi.org/10.1016/j.apcatb.2018.12.002>.

References

- [1] M.Z. Jacobson, M.A. Delucchi, G. Bazouin, Z.A.F. Bauer, C.C. Heavey, E. Fisher, S.B. Morris, D.J.Y. Piekutowski, T.A. Vencill, T.W. Yeskoo, Energy Environ. Sci. 8 (2015) 2093–2117.
- [2] J.H. Wu, Y. Huang, W. Ye, Y.G. Li, Adv. Sci. 4 (2017) 1700194.
- [3] H. Tong, S.X. Ouyang, Y.P. Bi, N. Umezawa, M. Oshikiri, J.H. Ye, Adv. Mater. 24 (2012) 229–251.
- [4] Y.F. Xu, M.Z. Yang, B.X. Chen, X.D. Wang, H.Y. Chen, D.B. Kuang, C.Y. Su, J. Am. Chem. Soc. 139 (2017) 5660–5663.
- [5] R. Long, Y. Li, Y. Liu, S.M. Chen, X.S. Zheng, C. Gao, C.H. He, N.S. Chen, Z.M. Qi, L. Song, J. Jiang, J.F. Zhu, Y.J. Xiong, J. Am. Chem. Soc. 139 (2017) 4486–4492.
- [6] D.D. Zhu, J.L. Liu, S.Z. Qiao, Adv. Mater. 28 (2016) 3423–3452.
- [7] W.G. Tu, Y. Zhou, Z.G. Zou, Adv. Mater. 26 (2014) 4607–4626.
- [8] S.J. Xie, Y. Wang, Q.H. Zhang, W.P. Deng, Y. Wang, ACS Catal. 4 (2014) 3644–3653.
- [9] H.J. Li, W.G. Tu, Y. Zhou, Z.G. Zou, Adv. Sci. 3 (2016) 1500389.
- [10] J. Wu, X.D. Li, W. Shi, P.Q. Ling, Y.F. Sun, X.C. Jiao, S. Gao, L. Liang, J.Q. Xu, W.S. Yan, C.M. Wang, Y. Xie, Angew. Chem. Int. Ed. 130 (2018) 8855–8859.
- [11] C.G. Zhou, J.K. Zhou, L. Lu, J.J. Wang, Z. Shi, B. Wang, L. Pei, S.C. Yan, Z.T. Yu,

- Z.G. Zou, Appl. Catal. B Environ. 237 (2018) 742–752.
- [12] X.G. Meng, S.X. Ouyang, T. Kako, P. Li, Q. Yu, T. Wang, J.H. Ye, Chem. Commun. 50 (2014) 11517–11519.
- [13] S.J. Xie, Y. Wang, Q.H. Zhang, W.Q. Fan, W.P. Deng, Y. Wang, Chem. Commun. 49 (2013) 2451–2453.
- [14] Q.Y. Li, L.L. Zong, C. Li, J.J. Yang, Appl. Surf. Sci. 314 (2014) 458–463.
- [15] L. Lu, B. Wang, S.M. Wang, Z. Shi, S.C. Yan, Z.G. Zou, Adv. Funct. Mater. 27 (2017) 1702447.
- [16] J.X. Low, C.J. Jiang, B. Cheng, S. Wageh, A.A.A. Ghamdi, J.G. Yu, Small Methods 1 (2017) 1700080.
- [17] S.M. Wang, Y. Guan, L. Lu, Z. Shi, S.C. Yan, Z.G. Zou, Appl. Catal. B Environ. 224 (2018) 10–16.
- [18] C.G. Zhou, S.M. Wang, Z.Y. Zhao, Z. Shi, S.C. Yan, Z.G. Zou, Adv. Funct. Mater. (2018) 1700080.
- [19] S.J. Yu, A.J. Wilson, J. Heo, P.K. Jain, Nano Lett. 18 (2018) 2189–2194.
- [20] S.W. Cao, B.J. Shen, T. Tong, J.W. Fu, J.G. Yu, Adv. Funct. Mater. 28 (2018) 1800136.
- [21] J. Zhang, H.P. Ma, Z.F. Liu, Appl. Catal. B Environ. 201 (2017) 84–91.
- [22] R. Long, K.K. Mao, M. Gong, S. Zhou, M. Zhi, Y. You, S. Bai, J. Jiang, Q. Zhang, X.J. Wu, Y.J. Xiong, Angew. Chem. Int. Ed. 53 (2014) 3205–3209.
- [23] L. Pino, A. Vita, M. Laganà, V. Recupero, Appl. Catal. B Environ. 148 (2014) 91–105.
- [24] S.H. Ahn, S.J. Yoo, H.J. Kim, D. Henkensmerier, A.W. Nam, S.K. Kim, J.H. Jang, Appl. Catal. B Environ. 180 (2016) 674–679.
- [25] L. Lu, S.M. Wang, C.G. Zhou, Z. Shi, H. Zhu, Z.Y. Xin, X.H. Wang, S.C. Yan, Z.G. Zou, J. Mater. Chem. A 6 (2018) 14838–14846.
- [26] H.X. Li, Z.F. Bian, J. Zhu, Y.N. Huo, Y.F. Lu, J. Am. Chem. Soc. 129 (2007) 4538–4539.
- [27] Y.Y. Liang, H.L. Wang, H.S. Casalongue, Z. Chen, H.J. Dai, Nano Res. 3 (2010) 701–705.
- [28] L. Liu, Y.H. Qi, J.R. Lu, S.L. Lin, W.J. An, Y.H. Liang, W.Q. Cui, Appl. Catal. B Environ. 183 (2016) 133–141.
- [29] X.B. Chen, L. Liu, Y. Peter, S.S. Mao, Science 331 (2011) 746.
- [30] X.X. Xu, C. Random, P. Efstathiou, J.T.S. Irvine, Nat. Mater. 11 (2012) 595.
- [31] G. Liu, L.C. Yin, J.Q. Wang, P. Niu, C. Zhen, Y.P. Xie, H.M. Cheng, Energy Environ. Sci. 5 (2012) 9603.
- [32] T. Minegishi, N. Nishimura, J. Kubota, K. Domen, Chem. Sci. 4 (2013) 595.
- [33] T. Hisatomi, T. Yamamoto, Q. Wang, T. Nakanishi, T. Higashi, M. Katayama, T. Minegishi, K. Domen, Catal. Sci. Technol. 8 (2018) 3918–3925.
- [34] Y. Cai, G. Zhang, Y.W. Zhang, Sci. Rep. 4 (2014) 6677.
- [35] Y. Liu, S. Zhou, J.M. Li, Y.J. Wang, G.Y. Jiang, Z. Zhao, B. Liu, X.Q. Gong, A.J. Duan, J. Liu, Y.C. Wei, L.Q. Zhang, Appl. Catal. B Environ. 168 (2015) 125–131.
- [36] X.G. Meng, T. Wang, L.Q. Liu, S.X. Ouyang, P. Li, H.L. Hu, T. Kako, H. Iwai, A. Tanaka, J.H. Ye, Angew. Chem. Int. Ed. 53 (2014) 11478–11482.
- [37] Z.W. Xiong, X.R. Chen, X.M. Wang, L.P. Peng, D.W. Yan, H.W. Lei, Y.J. Fu, J.B. Wu, Z.L. Li, X.Y. An, W.D. Wu, Appl. Surf. Sci. 268 (2013) 524–528.
- [38] H.M. Liu, T.D. Dao, L.Q. Liu, X.G. Meng, T. Nagaoka, J.H. Ye, Appl. Catal. B Environ. 209 (2017) 183–189.
- [39] S. Bai, J. Jiang, Q. Zhang, Y.J. Xiong, Chem. Soc. Rev. 44 (2015) 2893–2939.
- [40] G.Z. Xu, Z. Xu, Z. Shi, L. Pei, S.C. Yan, Z.G. Zou, ChemSusChem 10 (2017) 2897–2903.
- [41] X. Wang, X.Y. Liu, C.J. Tong, X.T. Yuan, W.J. Dong, T.Q. Lin, L.M. Liu, F.Q. Huang, J. Mater. Chem. A 4 (2016) 7762–7771.
- [42] Q.S. Pan, J. Peng, S. Wang, S.D. Wang, Catal. Sci. Tech. 4 (2014) 502–509.
- [43] W.Q. Wu, K. Bhattacharyya, K. Gray, E. Weitz, J. Phys. Chem. C 117 (2013) 20643–20655.
- [44] G. Zhou, H.R. Liu, K.K. Cui, A.P. Jia, G.S. Hu, Z.J. Jiao, X.M. Zhang, Appl. Surf. Sci. 383 (2016) 248–252.
- [45] Z.X. Sun, J.M.T.A. Fischer, Q. Li, J. Hu, Q.J. Tang, H.Q. Wang, Z.B. Wu, M. Hankel, D.J. Searles, L.Z. Wang, Appl. Catal. B Environ. 216 (2017) 146–155.